









# Accurate Distances of Massive Young Stars in the Scutum Spiral Arm

J. J. Li<sup>1</sup>, K. Immer<sup>2</sup>, M. J. Reid<sup>3</sup> , A. Sanna<sup>4,5</sup> , K. L. J. Rygl<sup>6</sup>, Y. Xu<sup>1</sup> , B. Zhang<sup>7</sup> , A. Brunthaler<sup>4</sup> , and K. M. Menten<sup>4</sup> <sup>1</sup>Purple Mountain Observatory, Chinese Academy of Sciences, Nanjing 210023, People's Republic of China; [jjli@pmo.ac.cn](mailto:jjli@pmo.ac.cn)<sup>2</sup>Joint Institute for VLBI ERIC, Oude Hoogeveensedijk 4, 7991 PD Dwingeloo, The Netherlands<sup>3</sup>Center for Astrophysics | Harvard & Smithsonian, 60 Garden Street, Cambridge, MA 02138, USA<sup>4</sup>Max-Planck-Institut für Radioastronomie, Auf dem Hügel 69, D-53121 Bonn, Germany<sup>5</sup>INAF, Osservatorio Astronomico di Cagliari, via della Scienza 5, I-09047 Selargius, Italy<sup>6</sup>Italian ALMA Regional Centre, INAF-Istituto di Radioastronomia, Via P. Gobetti 101, I-40129 Bologna, Italy<sup>7</sup>Shanghai Astronomical Observatory, Chinese Academy of Sciences, 80 Nandan Road, Shanghai 200030, People's Republic of China

Received 2022 March 6; revised 2022 July 15; accepted 2022 August 6; published 2022 September 27

## Abstract

As part of the BeSSeL Survey, we have used the Very Long Baseline Array to measure 16 trigonometric parallaxes and proper motions of molecular masers associated with 14 high-mass star-forming regions in the Scutum arm in the first quadrant of the Milky Way. This increases the number of maser sources with accurate distances in this arm to 42. The Scutum arm can now be traced over a length of  $\approx 8$  kpc and spanning  $\approx 100^\circ$  of Galactic azimuth. We find that the large inward peculiar motions noted by Immer et al. are concentrated near the end of the Galactic bar, while away from the bar modest peculiar motions more typical of spiral arms are seen, strengthening the suggestion that the large motions are induced by the bar.

*Unified Astronomy Thesaurus concepts:* [Trigonometric parallax \(1713\)](#)

## 1. Introduction

The Bar and Spiral Structure Legacy (BeSSeL) Survey uses the Very Long Baseline Array (VLBA) to study Galactic spiral structure by measuring the trigonometric parallaxes and proper motions of molecular masers associated with high-mass star-forming regions (HMSFRs; Reid et al. 2019). The Scutum arm lies between the Sagittarius and Norma arms in the first Galactic quadrant (Sato et al. 2014). At Galactic longitudes of  $\approx 30^\circ$  the Scutum arm passes near the end of the “long” bar (Wegg et al. 2015), where unusually large peculiar motions have been reported (Immer et al. 2019). Here we present measurements of trigonometric parallaxes and proper motions of 6.7 GHz CH<sub>3</sub>OH masers and a 22 GHz H<sub>2</sub>O maser associated with 14 HMSFRs, which increases the number of sources in the Scutum arm with accurate distances and three-dimensional motions to 42. These results provide a broader context for the anomalous motions and improve the case for their origin with the Galactic bar.

In Section 2, we briefly describe source selection and details regarding the observations and calibration of the VLBA data. We present the astrometric data used to fit for parallax and proper motion in Section 3. Finally, in Section 4, we locate the sources in the Milky Way, estimate their peculiar motions, and, when combined with previous results, provide a more comprehensive picture of the dynamics of the Scutum spiral arm.

## 2. Observations

Our observations used the VLBA operated by the National Radio Astronomy Observatory (NRAO<sup>8</sup>) and were performed under the programs of BR149 and BR198. Fifteen 6.7 GHz

CH<sub>3</sub>OH masers were observed with four 7 hr shared tracks spanning at least one year. One 22 GHz H<sub>2</sub>O maser was also observed at six epochs. The G028.39+00.08 water and methanol masers are almost certainly from the same giant molecular cloud and possibly associated with the same star, since their projected separation is only about 1' (0.02 pc at a distance of 4.3 kpc); see the detailed analysis of a similar source by Sanna et al. (2010). Also G010.32–00.15 and G010.34–00.14 are separated by 1/6 (1.4 pc at a distance of 2.9 kpc) and are likely tracing two young and massive stars within the same HMSFR. These sources were selected to likely be in the Scutum spiral arm, based on their Galactic longitudes, latitudes, and local standard of rest (LSR) velocities. We used the masers as the interferometer phase reference (i.e., inverse phase referencing, where the strong target instead of a weak calibrator source is used as the interferometer phase reference), since they were strong enough to yield  $>7\sigma$  detections in a single scan of 40 s on-source. Table 2 in the Appendix lists the details of the observed epochs. Owing to an electronics problem associated with sampling the antenna voltages, we discarded the first epoch of the BR198 observations and restarted the desired parallax sequence.

Four dual circularly-polarized bands of 16 MHz were observed and the band containing the masers was recorelated with 1000 and 2000 spectral channels for BR149 and BR198, respectively. For BR149 sources, the velocity resolution is  $0.36 \text{ km s}^{-1}$ , while for BR198 the corresponding value is  $0.18 \text{ km s}^{-1}$  for 6.7 GHz CH<sub>3</sub>OH masers and  $0.11 \text{ km s}^{-1}$  for the 22 GHz H<sub>2</sub>O maser. As described in detail in Reid et al. (2009) the correlated interferometric data were corrected for feed rotation, updated parameters of Earth's orientation, and position offsets from the catalog coordinates. Visibility amplitudes were converted to flux-density units using measured system temperatures and gain curves. Then electronic differences among frequency bands were removed using a single scan on a strong calibration source. Delay errors owing to the Earth's ionosphere were estimated from global ionospheric total electron content models and removed from the data. Next “geodetic-like blocks,” observations of multiple strong

<sup>8</sup> The National Radio Astronomy Observatory is a facility of the US National Science Foundation operated under cooperative agreement with Associated Universities, Inc.

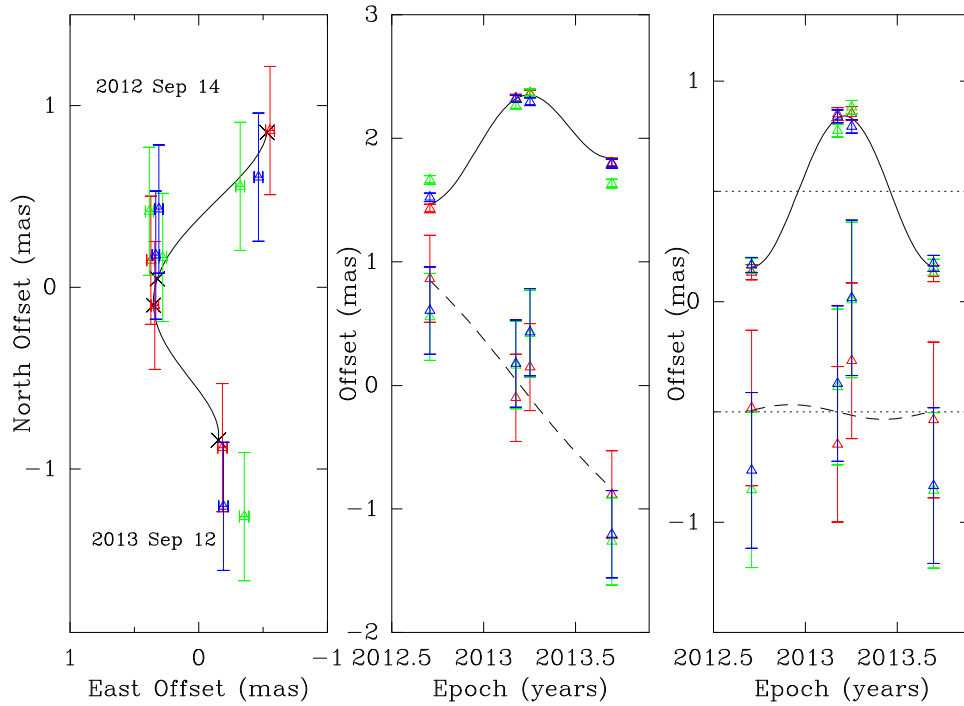


**Figure 1.** Parallax and proper-motion data and fits for G000.31–00.20. Plotted are position offsets for three maser spots at  $V_{\text{LSR}} = 15.5$  (red), 16.6 (green), and 18.4 (blue) calibrated relative to the background sources J1748–2907 and J1752–3001. Left panel: Positions on the sky with the first and last epochs labeled. Expected positions from the parallax and proper-motion fit are indicated (crosses). Middle panel: east (solid line) and north (dashed line) position offsets and best-fit parallax and proper motions vs. time. Right panel: same as the middle panel but with the best-fit proper motions removed to display only the parallax sinusoids.

**Table 1**  
Parallaxes and Proper Motions of Sources in the Scutum Arm

Source	$\ell$ (deg)	$b$ (deg)	Parallax (mas)	Distance (kpc)	$\mu_x$ (mas yr $^{-1}$ )	$\mu_y$ (mas yr $^{-1}$ )	$V_{\text{LSR}}$ (km s $^{-1}$ )
G000.31–00.20	0.31	–0.20	$0.342 \pm 0.042$	$2.9^{+0.4}_{-0.3}$	$0.21 \pm 0.39$	$-1.76 \pm 0.64$	$18 \pm 3$
G009.21–00.20	9.21	–0.20	$0.303 \pm 0.096$	$3.3^{+1.5}_{-0.8}$	$-0.41 \pm 0.45$	$-1.69 \pm 0.50$	$43 \pm 5$
G010.32–00.15	10.32	–0.15	$0.343 \pm 0.035$	$2.9^{+0.3}_{-0.3}$	$-1.03 \pm 0.36$	$-2.42 \pm 0.50$	$10 \pm 5$
G011.10–00.11	11.10	–0.11	$0.246 \pm 0.014$	$4.1^{+0.2}_{-0.2}$	$-0.23 \pm 0.38$	$-2.01 \pm 0.41$	$29 \pm 5$
G018.87+00.05	18.87	+0.05	$0.297 \pm 0.049$	$3.4^{+0.7}_{-0.5}$	$-0.17 \pm 0.32$	$-1.90 \pm 0.37$	$39 \pm 3$
G019.36–00.03	19.36	–0.03	$0.352 \pm 0.069$	$2.8^{+0.7}_{-0.5}$	$-1.12 \pm 0.38$	$-3.11 \pm 0.46$	$27 \pm 3$
G022.03+00.22	22.03	+0.22	$0.332 \pm 0.054$	$3.0^{+0.6}_{-0.4}$	$-0.06 \pm 0.26$	$-1.57 \pm 0.60$	$52 \pm 3$
G024.63–00.32	24.63	–0.32	$0.242 \pm 0.045$	$4.1^{+0.9}_{-0.6}$	$-0.31 \pm 0.27$	$-2.73 \pm 0.30$	$43 \pm 5$
G028.30–00.38	28.30	–0.38	$0.221 \pm 0.022$	$4.5^{+0.5}_{-0.4}$	$-1.62 \pm 0.23$	$-3.97 \pm 0.23$	$87 \pm 5$
G028.39+00.08	28.39	+0.08	$0.231 \pm 0.015$	$4.3^{+0.3}_{-0.3}$	$-1.40 \pm 0.24$	$-3.26 \pm 0.24$	$75 \pm 5$
G028.83–00.25	28.83	–0.25	$0.200 \pm 0.040$	$5.0^{+1.3}_{-0.8}$	$-1.89 \pm 0.22$	$-4.54 \pm 0.22$	$87 \pm 5$
G030.19–00.16	30.19	–0.16	$0.212 \pm 0.010$	$4.7^{+0.2}_{-0.2}$	$-2.08 \pm 0.22$	$-3.80 \pm 0.25$	$108 \pm 3$
G031.28+00.06	31.28	+0.06	$0.210 \pm 0.029$	$4.8^{+0.8}_{-0.6}$	$-1.99 \pm 0.19$	$-4.58 \pm 0.22$	$110 \pm 3$
G033.39+00.00	33.39	+0.00	$0.113 \pm 0.029$	$8.8^{+3.1}_{-1.8}$	$-2.48 \pm 0.13$	$-5.36 \pm 0.13$	$102 \pm 5$

**Note.** Columns 1, 2, and 3 give the source name, Galactic longitude, and latitude. Columns 4 and 5 give the measured parallax and inferred distance. Columns 6, 7, and 8 are the proper motion in the eastward ( $\mu_x = \mu_\alpha \cos \delta$ ) and northward directions ( $\mu_y = \mu_\delta$ ), and LSR velocity. Note that for G010.32–00.15 we give variance-weighted averages of G010.32–00.15 and G010.34–00.14; for G028.39+00.08 we give variance-weighted averages of its water and methanol maser parallaxes and its methanol maser proper motion; for G031.28+00.06 we give variance-weighted averages from this paper and Zhang et al. (2014).

calibrators with differing source elevations, were used to estimate and remove residual tropospheric delay errors. Finally, a single spectral channel of maser emission was used as the interferometer phase reference, greatly extending coherence times, and allowing Earth rotation synthesis maps to be made for all sources.

For each maser source, we used up to four background calibration sources, which were selected from the VCS2 and VCS3 catalogs (Fomalont et al. 2003; Petrov et al. 2005) and the BeSSeL calibrator surveys (Xu et al. 2006a; Immer et al. 2011). Table 3 in the Appendix presents the positions and

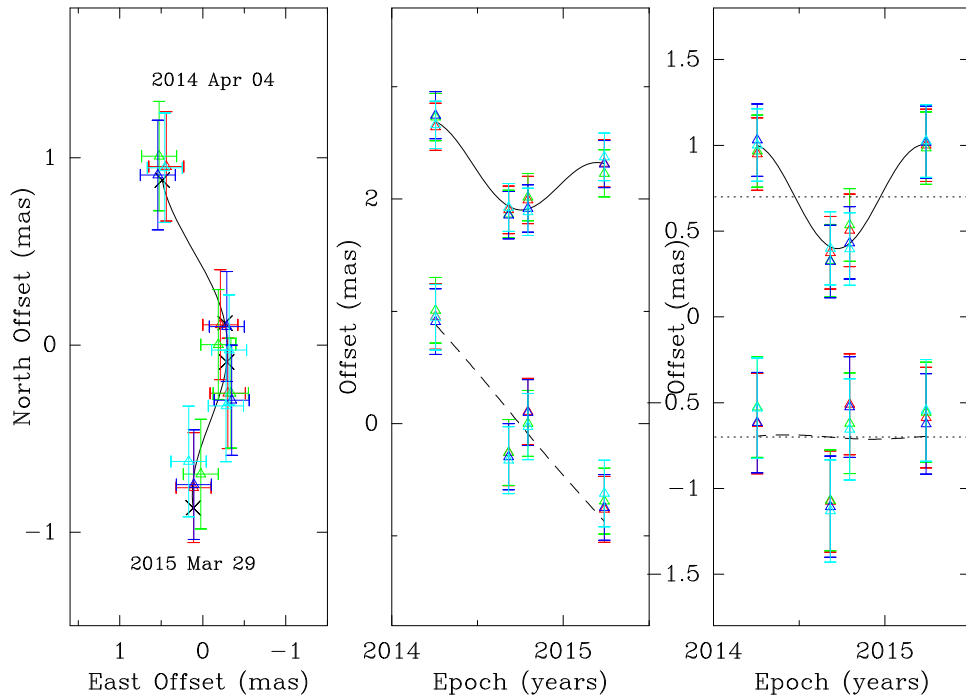


**Figure 2.** Parallax and proper-motion data and fits for G009.21–00.20. Plotted are position offsets for four maser spots at  $V_{\text{LSR}} = 40.5$  (red), 41.8 (green), 45.5 (blue), and 45.7 (cyan)  $\text{km s}^{-1}$  calibrated relative to the background sources J1755–2232, J1808–1822, and J1819–2036. A description of the three panels is given in the caption for Figure 1.

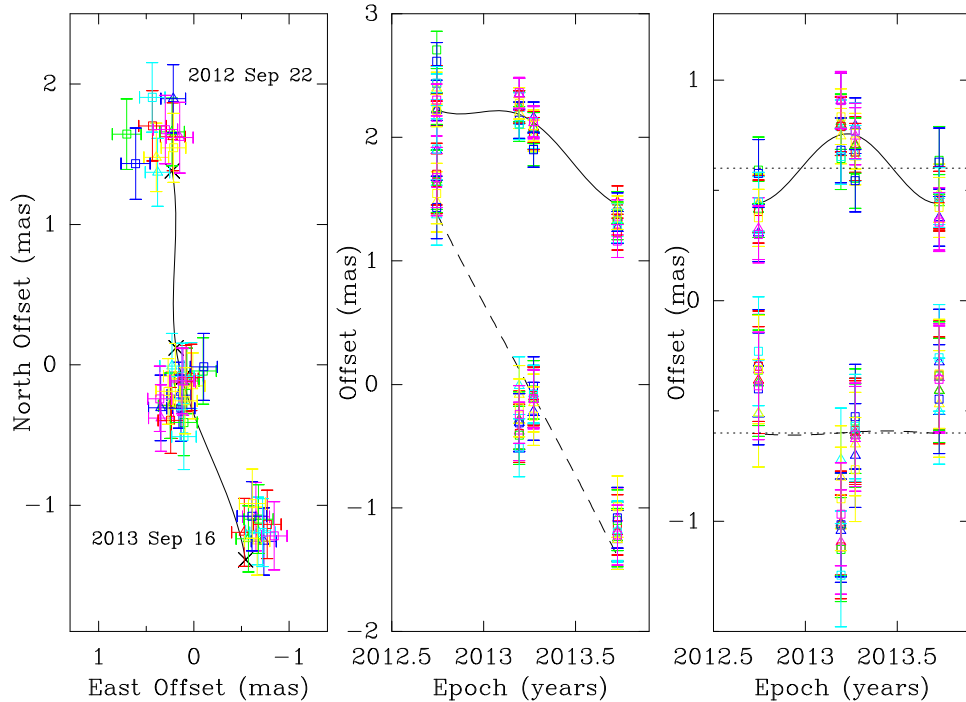


**Figure 3.** Parallax and proper-motion data and fits for G010.32–00.15. Plotted are position offsets for four maser spot at  $V_{\text{LSR}} = 4.1$  (red triangles), 4.5 (green triangles), 5.5 (blue triangles), 6.3 (cyan triangles), 6.6 (yellow triangles), 9.5 (magenta triangles), 9.8 (red squares), 10.2 (green squares), 10.5 (blue squares), 12.7 (cyan squares), 13.1 (yellow squares), and 13.4 (magenta squares)  $\text{km s}^{-1}$  calibrated relative to the background sources J1808–1822, J1821–2110, and J1751–1950, respectively. A description of the three panels is given in the caption for Figure 1.

intensity data of the maser spots used as the interferometer phase reference, the corresponding background sources, and other observational parameters.

### 3. Parallax and Proper-motion Results

The techniques used to fit parallax and proper motion for 22 GHz  $\text{H}_2\text{O}$  masers are straightforward and documented in

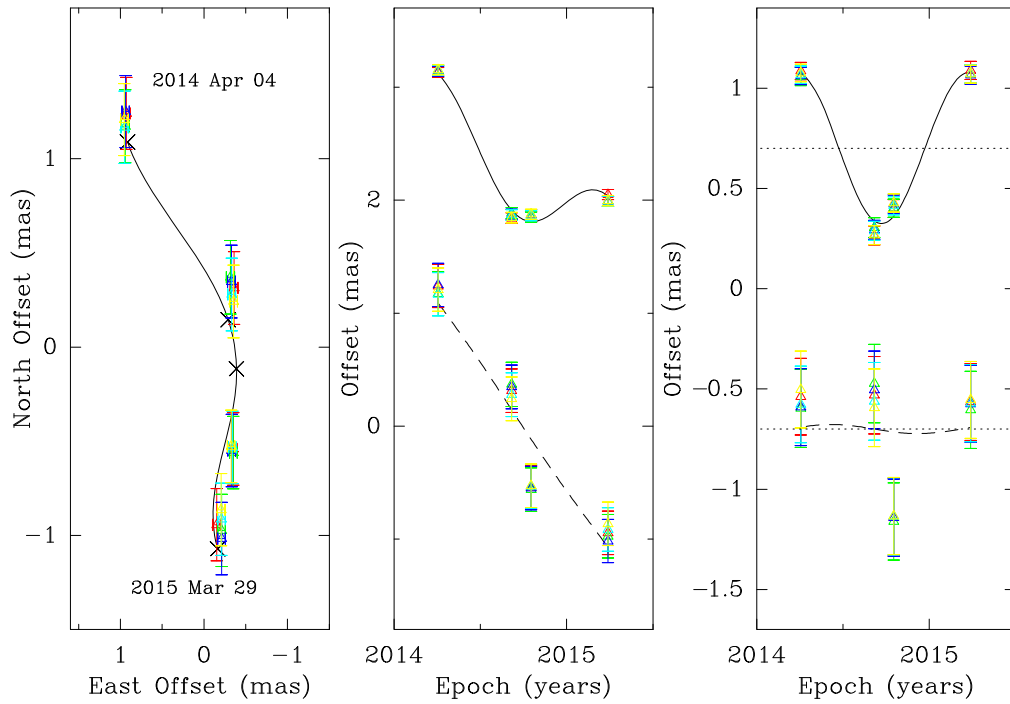


**Figure 4.** Parallax and proper-motion data and fits for G010.34–00.14. Plotted are position offsets for four maser spot at  $V_{\text{LSR}} = 4.9$  (red), 10.3 (green), 10.6 (blue), 12.8 (cyan), and 16.0 (yellow)  $\text{km s}^{-1}$  calibrated relative to the background sources J1808–1822, J1819–2036, and J1821–2110, respectively. A description of the three panels is given in the caption for Figure 1.

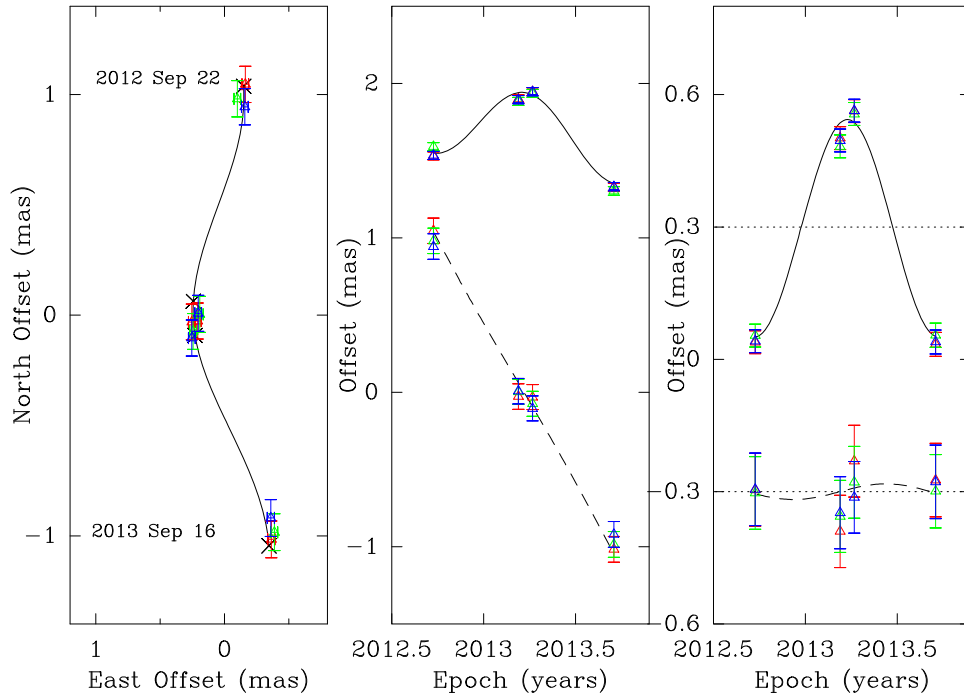


**Figure 5.** Parallax and proper-motion data and fits for G011.10–00.11. Plotted are position offsets for three maser spot at  $V_{\text{LSR}} = 29.8$  (red), 30.2 (green), and 32.0 (blue)  $\text{km s}^{-1}$  calibrated relative to the background sources J1751–1950 and J1821–2110, respectively. A description of the three panels is given in the caption for Figure 1.

Reid et al. (2009). However, for 6.7 GHz  $\text{CH}_3\text{OH}$  masers, we found that ionospheric “wedges” cause dispersive delay errors, which are direction dependent and can significantly limit astrometric accuracy (Reid et al. 2017). Methods to mitigate these effects have improved and now involve fitting parallax and proper-motion parameters simultaneously with a two-

dimensional “tilted plane” to the relative positions of quasars that surround a target maser at each epoch (Zhang et al. 2019). The best-fitted results are presented in Table 1. Note that for G010.32–00.15 we give variance-weighted averages of the G010.32–00.15 and G010.34–00.14 parallaxes and proper motions. For G028.39+00.08 we give variance-weighted

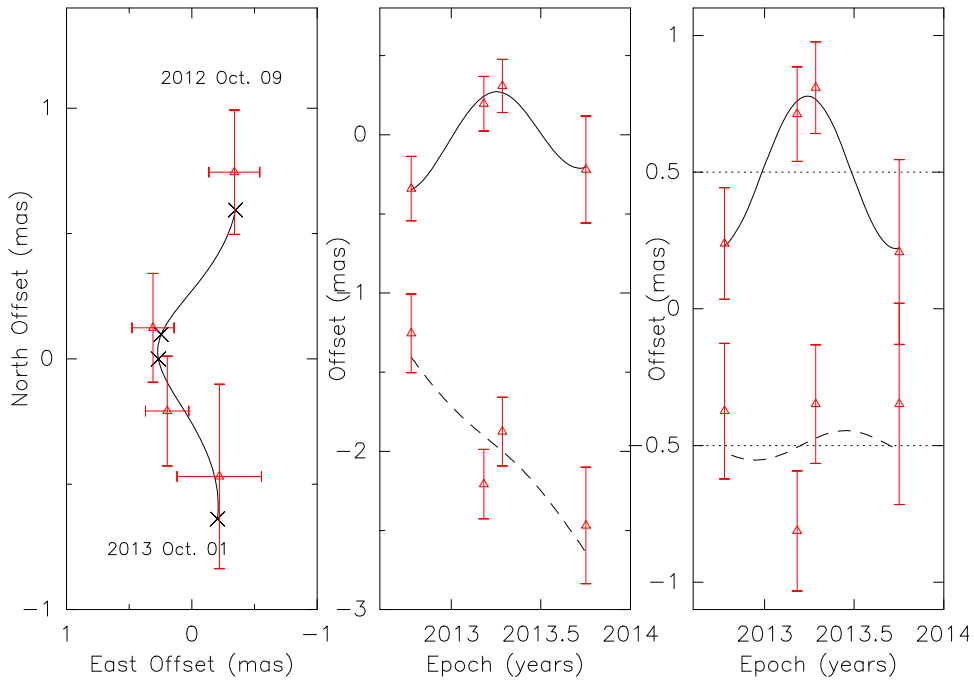


**Figure 6.** Parallax and proper-motion data and fits for G018.87+00.05. Plotted are position offsets for one maser spot at  $V_{\text{LSR}} = 38.3$  (red)  $\text{km s}^{-1}$  calibrated relative to the background source J1821–1224. A description of the three panels is given in the caption for Figure 1.

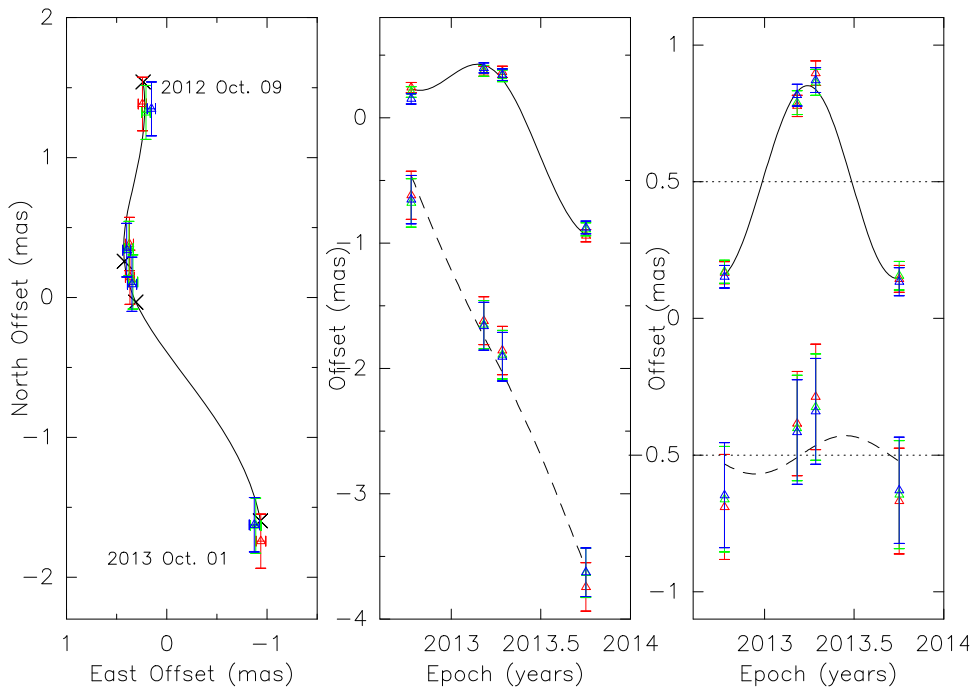


**Figure 7.** Parallax and proper-motion data and fits for G019.36–00.03. Plotted are position offsets for three maser spots at  $V_{\text{LSR}} = 25.4$  (red), 27.2 (green), and 28.6 (blue)  $\text{km s}^{-1}$  calibrated relative to the background source J1821–1224. A description of the three panels is given in the caption for Figure 1.

averages of the water and methanol masers’ parallax and use the methanol maser proper motion as this source’s proper motion, since water masers can form in molecular outflows of several tens of kilometers per second. The parallax of HMSFR G031.28+00.06 was measured with 12.2 GHz methanol maser observations (Zhang et al. 2014); here we give variance-weighted averages from this paper and Zhang et al. (2014). More details are presented in Tables 4 and 5 in the Appendix. Figures 1–16 show the positions and fits of the maser spots

(relative to the background sources) as a function of time.

As done in previous work for the BeSSeL survey (Reid et al. 2014, 2019), the association of masers with spiral arms was primarily based on matching positions and LSR velocities with arms identified in  $l$ – $V$  plots of CO emission (Dame et al. 2001). When possible, we report the average motion of multiple maser spots as an estimate of the motion of the central massive star. Methanol masers are preferred signposts of massive stars, such as

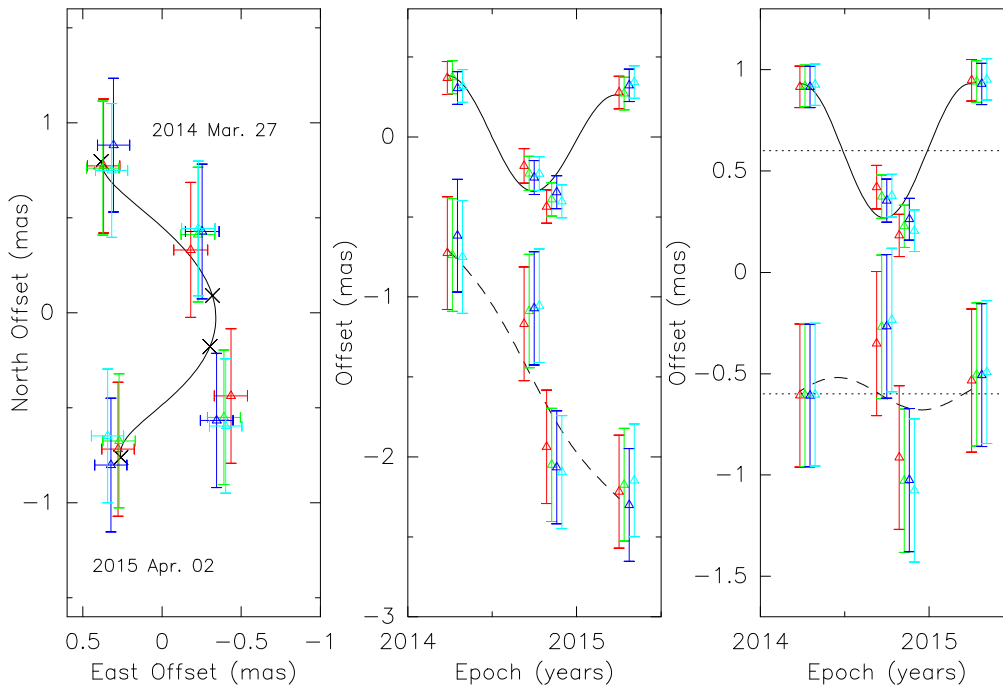


**Figure 8.** Parallax and proper-motion data and fits for G022.03+00.22. Plotted are position offsets for four maser spots at  $V_{\text{LSR}} = 49.5$  (red), 51.7 (green), 53.3 (blue), and 54.4 (cyan)  $\text{km s}^{-1}$  calibrated relative to the background source J1825–0737. A description of the three panels is given in the caption for Figure 1.

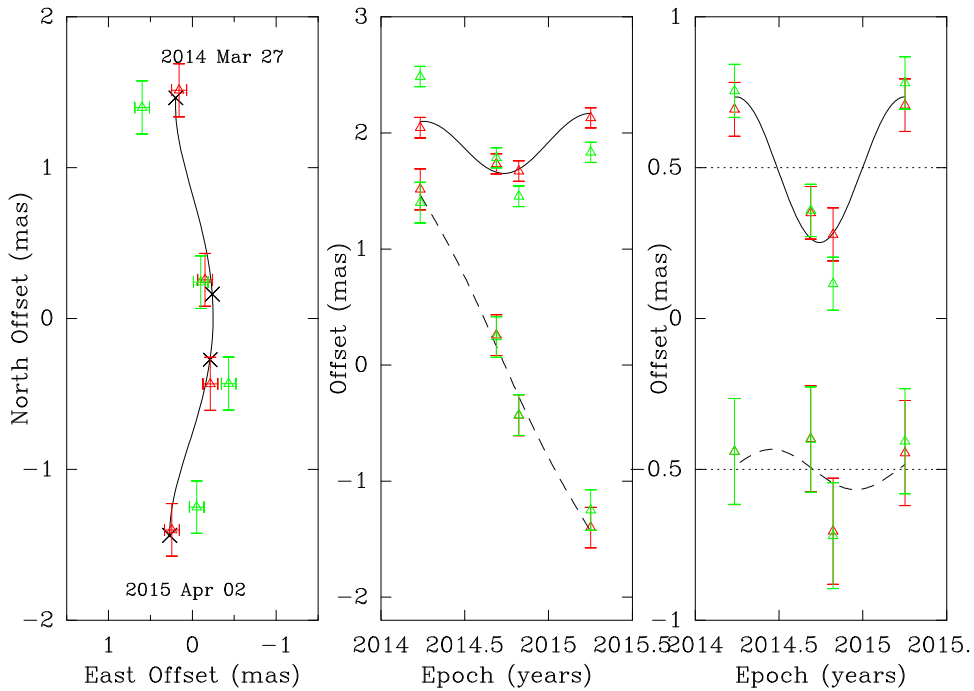


**Figure 9.** Parallax and proper-motion data and fits for G024.63–00.32. Plotted are position offsets for two maser spots at  $V_{\text{LSR}} = 35.7$  (red) and 48.1 (green)  $\text{km s}^{-1}$  calibrated relative to the background sources J1825–0737 and J1846–0651. A description of the three panels is given in the caption for Figure 1.

the archetypal source W3OH (Xu et al. 2006b), and typically trace molecular material slowly expanding at  $\sim 5 \text{ km s}^{-1}$  (Moscadelli et al. 2002). For sources with multiple maser spots, we adopt a  $\pm 3 \text{ km s}^{-1}$  uncertainty for each velocity component and add this in quadrature with formal motion uncertainties. For cases in which we only measure one spot we adopt a  $5 \text{ km s}^{-1}$  uncertainty.

#### 4. Discussion

Previously, there were 29 parallaxes for sources in the Scutum arm reported by the BeSSeL Survey (Sato et al. 2014; Immer et al. 2019) and the VERA project (VERA Collaboration et al. 2020). With the 13 new sources (G031.28+00.06 had a previous measurement) reported here, there are now 42

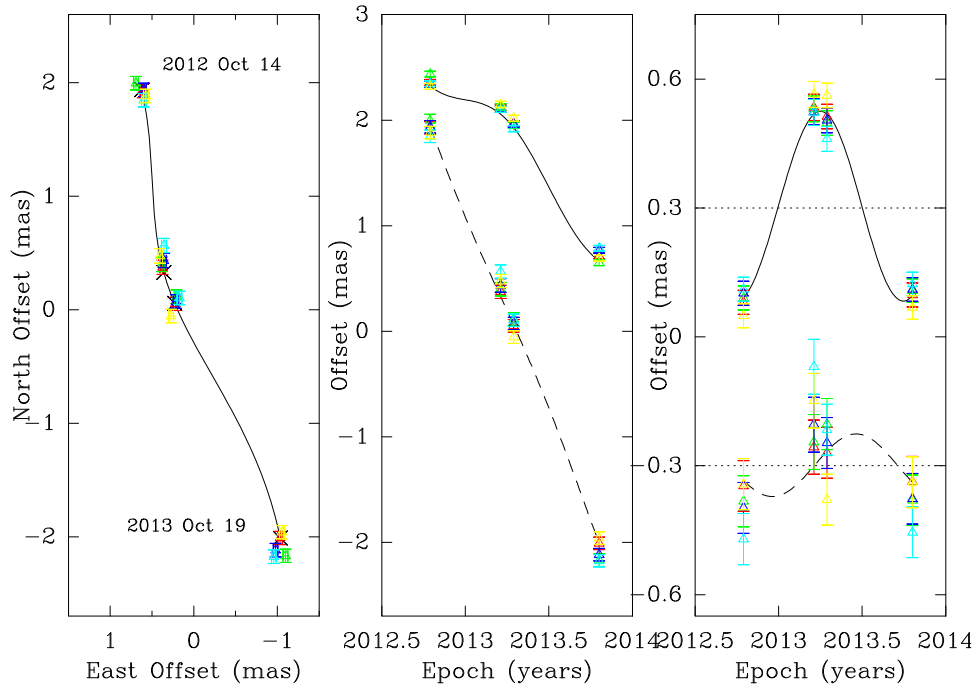


**Figure 10.** Parallax and proper-motion data and fits for G028.30–00.38. Plotted are position offsets for five maser spots at  $V_{\text{LSR}} = 81.3$  (red), 82.0 (green), 82.4 (blue), 92.4 (cyan), and 93.9 (yellow)  $\text{km s}^{-1}$  calibrated relative to the background sources J1833–0323, J1834–0301, and J1846–0651. A description of the three panels is given in the caption for Figure 1.

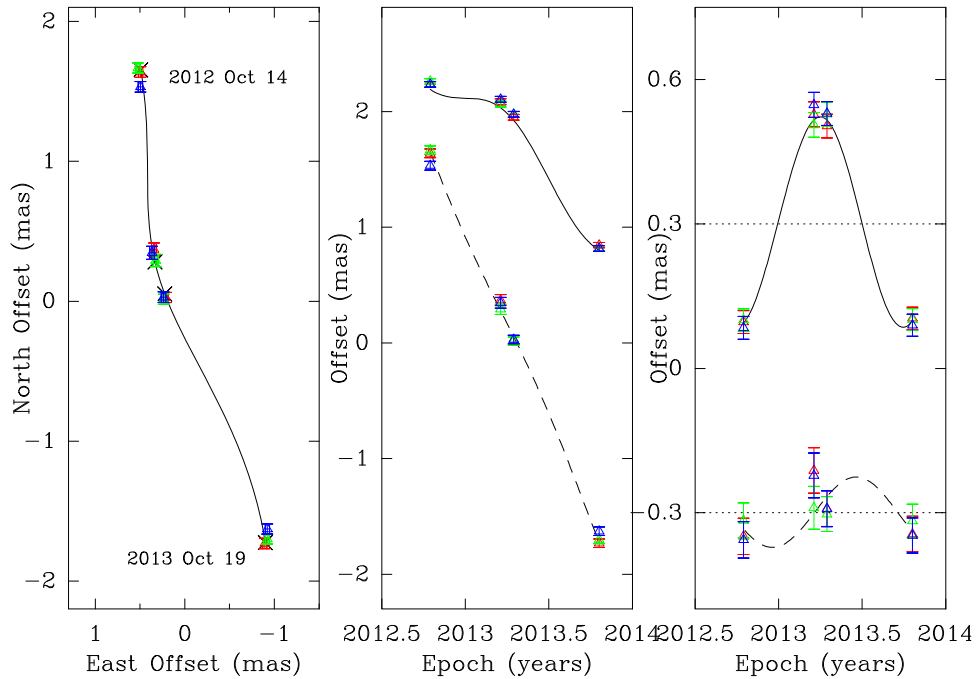


**Figure 11.** Parallax and proper-motion data and fits for G028.39+00.08 with methanol masers. Plotted are position offsets for three maser spots at  $V_{\text{LSR}} = 69.1$  (red), 71.3 (green), and 81.7 (blue)  $\text{km s}^{-1}$  calibrated relative to the background sources J1833–0323, J1834–0301, and J1846–0651. A description of the three panels is given in the caption for Figure 1.

HMSFRs, which better trace the structure of the Scutum arm in the first and fourth Galactic quadrants. Figure 17 displays the locations and peculiar motions of sources in the Scutum–Centaurus arm (blue symbols) with fractional parallax accuracy better than  $\pm 20\%$ , along with sources in other spiral arms from Reid et al. (2019). We now trace the arm over a length of

$\approx 8$  kpc covering a range of Galactic azimuth of  $\approx 100^\circ$ . These results were used by Reid et al. (2019) to characterize the Scutum arm’s pitch angle (between  $12^\circ$  and  $14^\circ$ ) and width ( $230 \pm 50$  pc) at a Galactocentric radius of 4.9 kpc.

The peculiar (i.e., noncircular) motions were calculated from the three-dimensional velocity vectors, obtained for each

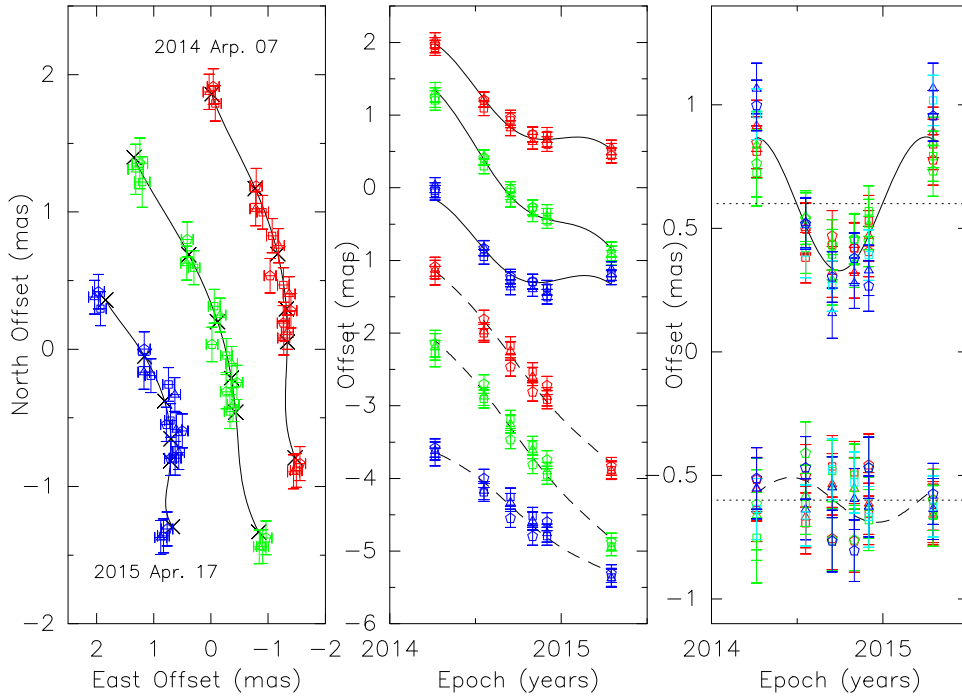


**Figure 12.** Parallax and proper-motion data and fits for G028.39+00.08 with water masers. Plotted are position offsets for three maser spots at  $V_{\text{LSR}} = 77.5$  (red), 77.6 (green), and 78.7 (blue)  $\text{km s}^{-1}$  calibrated relative to the background sources J1833–0323 (triangles), J1834–0301 (squares), and J1846–0651 (pentagons). A description of the three panels is given in the caption for Figure 1.

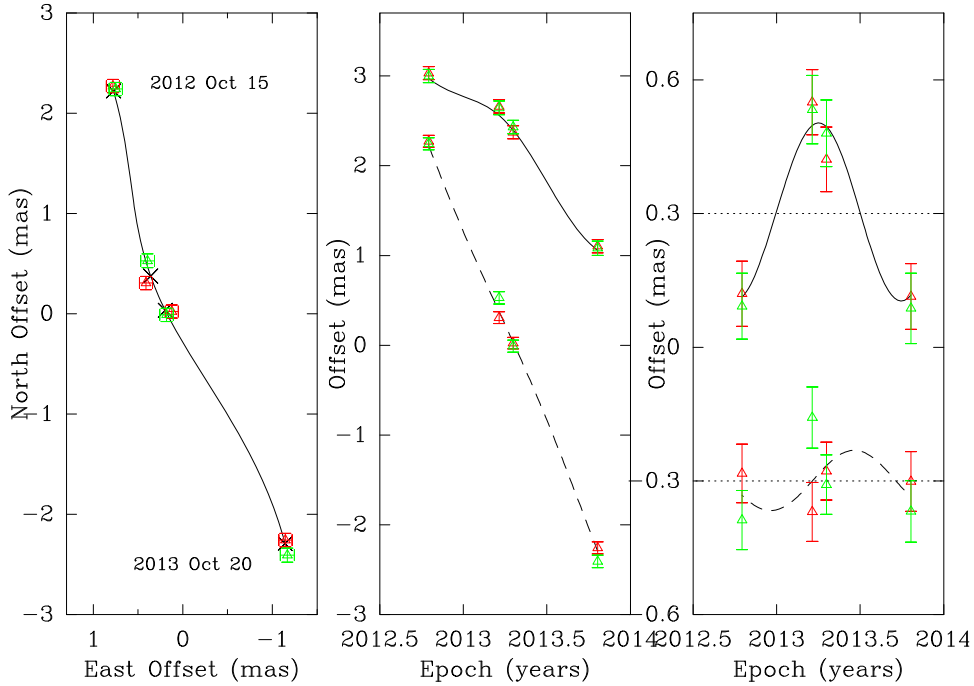


**Figure 13.** Parallax and proper-motion data and fits for G028.83–00.25. Plotted are position offsets for two maser spots at  $V_{\text{LSR}} = 90.8$  (red) and 81.1 (green)  $\text{km s}^{-1}$  calibrated relative to the background sources J1833–0323, J1834–0301, J1846–0651, and J1853–0048. A description of the three panels is given in the caption for Figure 1.

source from its  $V_{\text{LSR}}$ , two proper-motion components, source coordinates, and parallax distance. In order to remove circular rotation, we adopted the distance to the Galactic center,  $R_0$ , of 8.15 kpc, the circular rotation speed at the Sun,  $\Theta_0$ , of 236  $\text{km s}^{-1}$ , and the Galactic rotation curve from Reid et al. (2019). Immer et al. (2019) noted that many sources in the

Scutum arm have anomalous peculiar motions of up to  $\approx 50 \text{ km s}^{-1}$ , mostly directed toward the Galactic center. These sources were clustered near the end of the Galactic bar. Here we expand on this finding by testing whether or not these anomalous peculiar motions are found throughout the Scutum arm or only near the end of the bar. The left panel in Figure 18



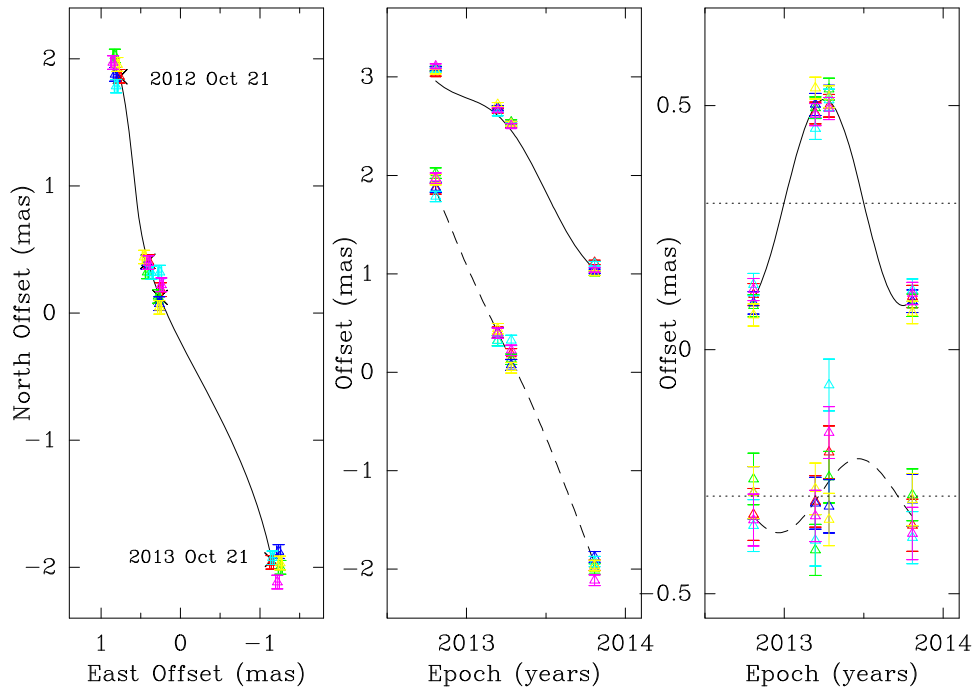


**Figure 14.** Parallax and proper-motion data and fits for G030.19–00.16. Plotted are position offsets for three maser spots at  $V_{\text{LSR}} = 104.8$  (red), 108.4 (green), and 110.2 (magenta)  $\text{km s}^{-1}$ , and three other maser spots (blue, cyan, and yellow) at  $109.4 \text{ km s}^{-1}$  calibrated relative to the background sources J1834–0301, J1846–0003, J1853–0048, and J1857–0048. A description of the three panels is given in the caption for Figure 1.

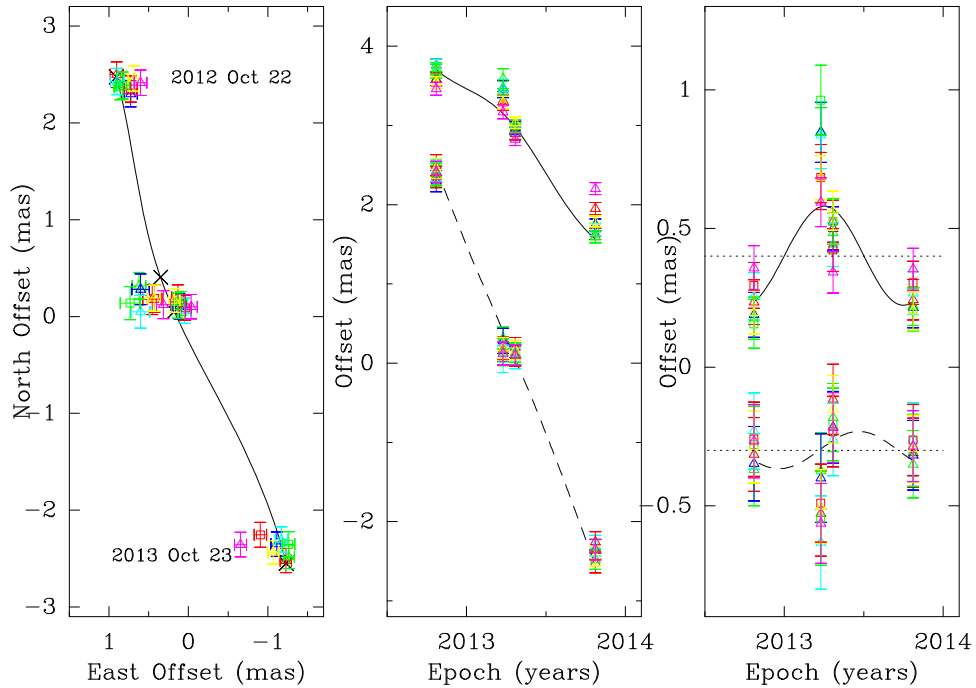


**Figure 15.** Parallax and proper-motion data and fits for G031.28+00.06. Plotted are position offsets for six maser spots at  $V_{\text{LSR}} = 105.7$  (red triangles), 106.0 (green triangles), 107.5 (blue triangles), 110.0 (cyan triangles), 110.7 (yellow triangles), and 111.1 (magenta triangles)  $\text{km s}^{-1}$  and two maser spots (red and green squares) at  $110.4 \text{ km s}^{-1}$ , calibrated relative to the background sources J1834–0301, J1846–0003, J1853–0048, and J1857–0048. A description of the three panels is given in the caption for Figure 1.

presents binned averages of the component of peculiar motions toward the Galactic center ( $U$ ) as a function of Galactocentric azimuth. Bins are  $10^\circ$  in azimuth and we only plot bins containing two or more sources. This shows that the large ( $>20 \text{ km s}^{-1}$ ) peculiar motions toward the Galactic center are

confined to an azimuth range of  $15^\circ$ – $35^\circ$ , and adds evidence to the suggestion by Immer et al. (2019) that these peculiar motions are induced by the Galactic bar. For comparison, the right panel of Figure 18 plots binned averages of the component of peculiar motions in the direction of Galactic rotation ( $V$ ) as a function

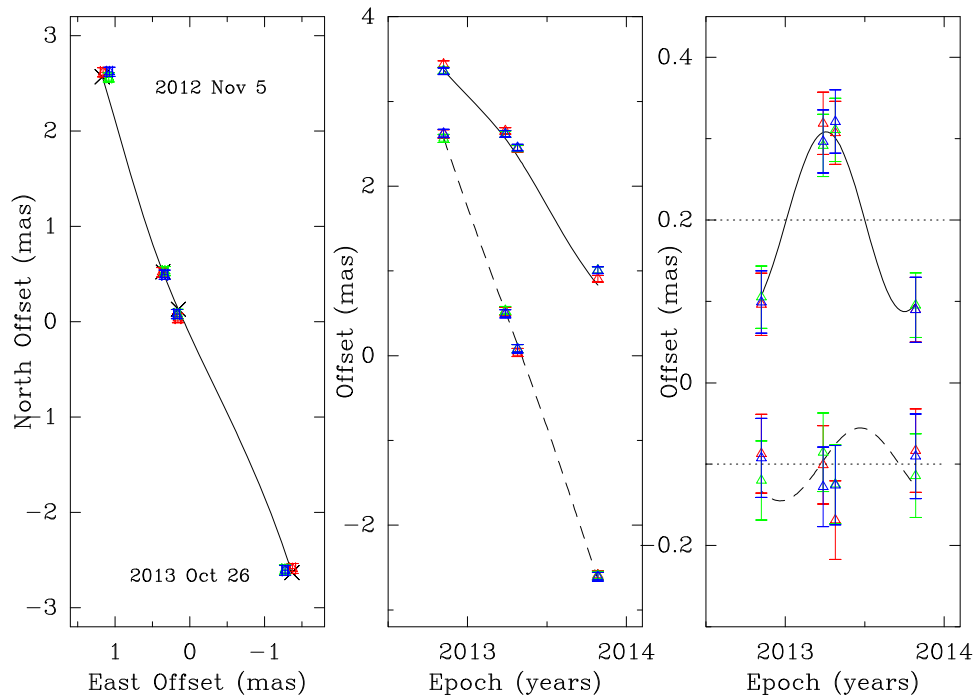


**Figure 16.** Parallax and proper-motion data and fits for G033.39+00.00. Plotted are position offsets for three maser spots at  $V_{\text{LSR}} = 98.2$  (red), 105.4 (green), and 106.1 (blue)  $\text{km s}^{-1}$  calibrated relative to the background sources J1846–0003, J1848+0138, and J1853–0048. A description of the three panels is given in the caption for Figure 1.

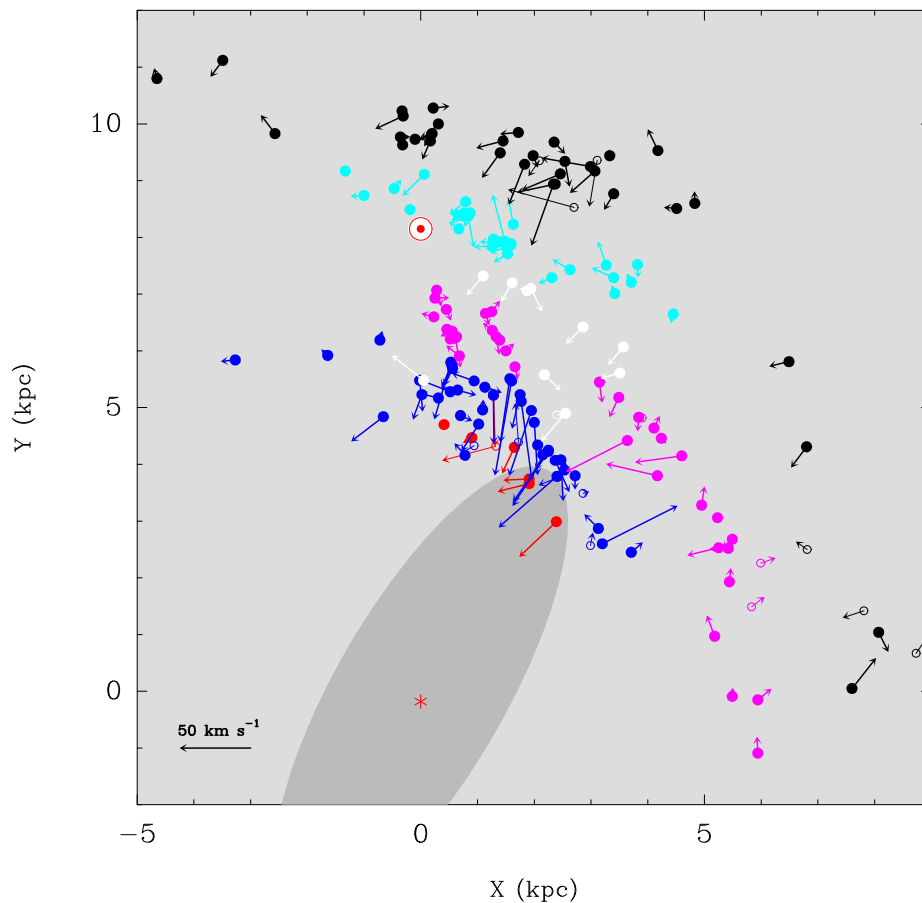


**Figure 17.** Peculiar (noncircular) motions of massive young stars in the Milky Way, updated from Figure 6 of Reid et al. (2019). The Galactic center (red asterisk) is at (0,0) and the Sun (red Sun symbol) is at (0.8,1.5) kpc. A schematic “long” bar from Wegg et al. (2015) is indicated by the shaded ellipse. Filled and open circles indicate sources with peculiar motion uncertainties less than 25 and 50  $\text{km s}^{-1}$ , and sources with larger uncertainties are not plotted. Sources in the Scutum–Centaurus arm are indicated by blue symbols; other arms shown are the Norma arm (red), Sagittarius–Carina arm (magenta), Local Arm (cyan), and Perseus arm (black). White symbols are either interarm or unassigned sources. As noted by Immer et al. (2019) there are large peculiar motions toward the Galactic center for many sources in the Scutum–Centaurus arm, as well as a smaller number in the Norma and Sagittarius–Carina arms, near the end of the Galactic bar.

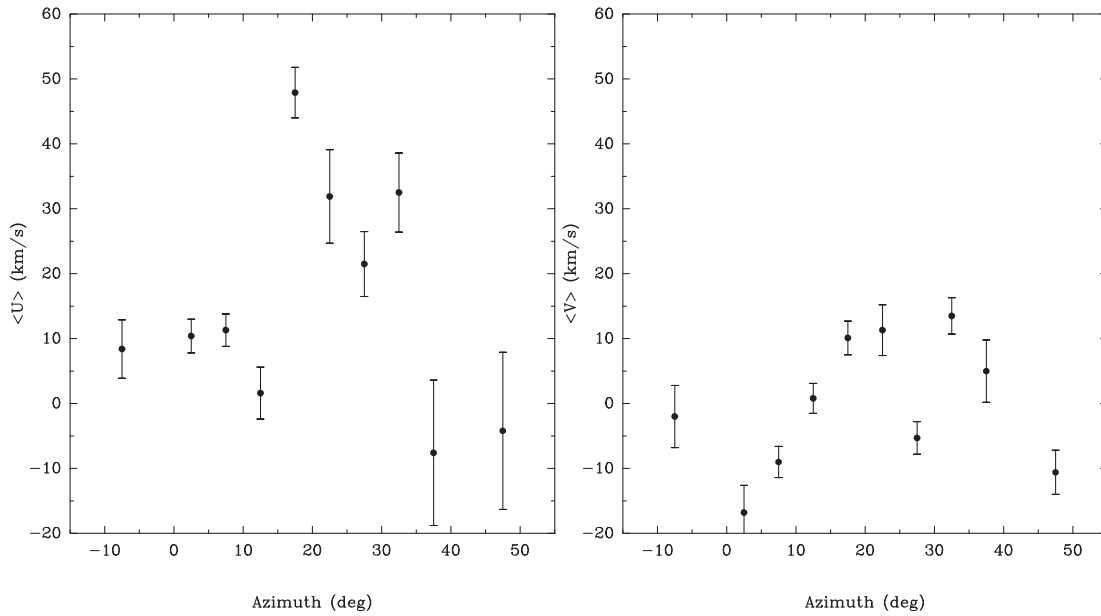


**Figure 18.** Histograms binned in Galactocentric azimuth of components of the peculiar motions in the Scutum–Centaurus arm. Variance-weighted values in each bin are plotted against Galactocentric azimuth. Bins are  $10^\circ$  wide and only bins containing two or more points are plotted. Left panel:  $U$ -component of peculiar motion (positive toward the Galactic center). Right panel:  $V$ -component of peculiar motion (positive in the direction of Galactic rotation). Note that the large positive ( $U$ ) values are confined to azimuths between  $15^\circ$  and  $35^\circ$  and are not evident throughout the arm, whereas the magnitudes of the ( $V$ ) values are considerably smaller between those azimuths.

of Galactocentric azimuth. In contrast to the average  $U$  values in the left panel, the magnitudes of the average  $V$  values are all less than  $20 \text{ km s}^{-1}$ , suggesting that the effects of the bar on peculiar motions are predominantly toward the Galactic center.

In Figure 17 one can see a small number of sources with large peculiar motions toward the Galactic center in the Norma arm (red symbols), which lies just inward of the Scutum arm. More data for the Norma arm sources would be needed to perform the same analysis as just presented for the Scutum arm. At much greater Galactic radii ( $\approx 9 \text{ kpc}$ ), there are some large peculiar motions roughly toward the Galactic center in the Perseus arm between longitudes of  $100^\circ$  and  $140^\circ$ , first noted by Xu et al. (2006b). These could be related to a resonance (e.g., the outer Linblad resonance) with the bar. If, for example, the Scutum arm is associated with the inner Linblad resonance,

then one would not expect anomalous peculiar motions for sources between the Scutum and Perseus arms.

This work was funded by the NSFC grants 11933011, 11873019, 11673066, 11988101, and the Key Laboratory for Radio Astronomy.

*Facility:* VLBA.

## Appendix A Observations

Table 2 lists observation frequencies and dates. Table 3 presents the positions and intensity data of the maser spots used as the interferometer phase reference, the corresponding background sources, and other observational parameters.

**Table 2**  
Details of the Epochs Observed

Code	GHz	Source	Epoch 1	Epoch 2	Epoch 3	Epoch 4	Epoch 5	Epoch 6	Epoch 7
BR149B	6.7	G000.31–00.20	2012 Sep 14	2013 Mar 5	2013 Apr 2	2013 Sep 12	...	...	...
BR149C	6.7	G010.32–00.15	2012 Sep 22	2013 Mar 10	2013 Apr 7	2013 Sep 16	...	...	...
		G011.10–00.11	2012 Sep 22	2013 Mar 10	2013 Apr 7	2013 Sep 16	...	...	...
BR149F	6.7	G018.87+00.05	2012 Oct 9	2013 Mar 7	2013 Apr 14	2013 Oct 1	...	...	...
		G019.36–00.03	2012 Oct 9	2013 Mar 7	2013 Apr 14	2013 Oct 1	...	...	...
BR149H	6.7	G028.30–00.38	2012 Oct 14	2013 Mar 18	2013 Apr 16	2013 Oct 19	...	...	...
		G028.39+00.08	2012 Oct 14	2013 Mar 18	2013 Apr 16	2013 Oct 19	...	...	...
BR149I	6.7	G028.83–00.25	2012 Oct 15	2013 Mar 19	2013 Apr 19	2013 Oct 20	...	...	...
BR149J	6.7	G030.19–00.16	2012 Oct 21	2013 Mar 23	2013 Apr 18	2013 Oct 21	...	...	...
BR149K	6.7	G031.28–00.06	2012 Oct 22	2013 Mar 25	2013 Apr 22	2013 Oct 23	...	...	...
BR149M	6.7	G033.39+00.00	2012 Nov 5	2013 Mar 28	2013 Apr 25	2013 Oct 26	...	...	...
BR198E	6.7	G009.21–00.20	[2013 Sep 13]	2014 Apr 4	2014 Sep 6	2014 Oct 17	2015 Mar 29	...	...
		G010.34–00.14	[2013 Sep 13]	2014 Apr 4	2014 Sep 6	2014 Oct 17	2015 Mar 29	...	...
BR198H	6.7	G022.03+00.22	[2013 Oct 2]	2014 Mar 27	2014 Sep 8	2014 Oct 27	2015 Apr 2	...	...
		G024.63–00.32	[2013 Oct 2]	2014 Mar 27	2014 Sep 8	2014 Oct 27	2015 Apr 2	...	...
BR198L	22	G028.39+00.08	[2013 Nov 4]	2014 Apr 7	2014 Jul 20	2014 Sep 14	2014 Oct 31	2014 Dec 1	2015 Apr 17

**Note.** Epochs in square brackets were not used owing to electronic failures.

**Table 3**  
Positions and Brightnesses

Source	R.A. (J2000) ( <sup>h</sup> <sup>m</sup> <sup>s</sup> )	Decl. (J2000) ( <sup>°</sup> <sup>'</sup> <sup>"</sup> )	$\phi$ (deg)	Brightness (Jy beam <sup>-1</sup> )	$V_{\text{LSR}}$ (km s <sup>-1</sup> )	NW beam (mas, mas, deg)
G000.31–00.20	17 47 09.1088	–28 46 16.314		12.4	18.3	4.6 × 3.2 @ 12
J1748–2907	17 48 45.6836	–29 07 39.405	0.5	0.022		4.6 × 3.8 @ 4
J1752–3001	17 52 30.9499	–30 01 06.690	1.7	0.065		4.7 × 3.4 @ 10
G009.21–00.20	18 06 52.8421	–21 04 27.878		2.7	41.8	5.2 × 3.8 @ 40
J1819–2036	18 19 36.8956	–20 36 31.575	3.0	0.030		6.2 × 4.0 @ 30
J1755–2232	17 55 26.2846	–22 32 10.617	3.0	0.153		8.1 × 4.1 @ 28
J1808–1822	18 08 55.5155	–18 22 53.393	2.7	0.052		7.6 × 4.0 @ 29
G010.32–00.15	18 09 01.4524	–20 05 07.761		12.8	11.6	6.0 × 2.8 @ –4
J1808–1822	18 08 55.5154	–18 22 53.397	1.7	0.035		7.4 × 2.4 @ –12
J1821–2110	18 21 05.4693	–21 10 45.252	3.0	0.044		7.2 × 2.7 @ –6
J1751–1950	17 51 41.3438	–19 50 47.504	4.1	0.023		6.0 × 3.1 @ –3
G010.34–00.14	18 08 59.9836	–20 03 35.380		7.8	16.1	7.9 × 3.8 @ 27
J1808–1822	18 08 55.5154	–18 22 53.396	1.7	0.058		8.7 × 3.9 @ 29
J1819–2036	18 19 36.8956	–20 36 31.578	3.0	0.037		8.6 × 4.2 @ 26
J1821–2110	18 21 05.4694	–21 10 45.255	3.0	0.056		9.6 × 4.0 @ 25
G011.10–00.11	18 10 28.2470	–19 22 30.210		5.6	32.3	5.8 × 3.1 @ –2
J1821–2110	18 21 05.4695	–21 10 45.246	3.1	0.062		6.3 × 3.0 @ –5
J1751–1950	17 51 41.3438	–19 50 47.499	4.5	0.041		6.3 × 3.0 @ –5
G018.87+00.05	18 25 11.3528	–12 27 36.545		2.4	38.3	6.3 × 3.3 @ 17
J1821–1224	18 21 23.27826	–12 24 12.9142	0.9	0.014		6.6 × 3.4 @ 19
G019.36–00.03	18 26 25.7790	–12 03 53.263		5.1	25.4	4.2 × 2.5 @ –7
J1821–1224	18 21 23.2783	–12 24 12.907	1.3	0.012		4.9 × 2.2 @ –2
G022.03+0.22	18 30 34.69980	–09 34 47.0076		2.8	54.4	5.0 × 2.8 @ 10
J1825–0737	18 25 37.6097	–07 37 30.014	2.3	0.284		4.8 × 2.8 @ 13
G024.63–0.32	18 37 22.70946	–07 31 42.1160		0.862	48.1	7.7 × 3.0 @ 40
J1846–0651	18 46 06.3007	–06 51 27.746	2.3	0.016		7.7 × 3.0 @ 40
J1825–0737	18 25 37.6096	–07 37 30.013	2.9	0.182		5.0 × 3.1 @ 13
G028.30–00.38	18 44 21.96742	–04 17 39.9149		6.7	81.3	4.1 × 2.2 @ –9
J1833–0323	18 33 23.9050	–03 23 31.445	2.9	0.052		3.9 × 2.4 @ –12
J1834–0301	18 34 14.0746	–03 01 19.626	2.8	0.081		4.4 × 2.0 @ –5
J1846–0651	18 46 06.3004	–06 51 27.747	2.6	0.033		4.0 × 2.4 @ –11
G028.39+00.08 <sup>a</sup>	18 42 51.98220	–03 59 54.4959		2.8	71.3	4.9 × 2.5 @ –5
J1834–0301	18 34 14.0746	–03 01 19.629	2.4	0.089		4.8 × 2.4 @ –5
J1833–0323	18 33 23.9049	–03 23 31.447	2.4	0.051		4.7 × 2.4 @ –4
J1846–0651	18 46 06.3004	–06 51 27.749	3.0	0.032		5.0 × 2.4 @ –5
G028.39+00.08 <sup>b</sup>	18 42 51.97590	–03 59 53.6630		68.9	77.6	1.7 × 1.3 @ 25

**Table 3**  
(Continued)

Source	R.A. (J2000) ( <sup>h</sup> <sup>m</sup> <sup>s</sup> )	Decl. (J2000) ( <sup>°</sup> <sup>'</sup> <sup>''</sup> )	$\phi$ (deg)	Brightness (Jy beam <sup>-1</sup> )	$V_{\text{LSR}}$ (km s <sup>-1</sup> )	NW beam (mas, mas, deg)
J1834-0301	18 34 14.0748	-03 01 19.629	2.4	0.055		2.0 × 1.2 @ 35
J1833-0323	18 33 23.9049	-03 23 31.447	2.4	0.037		2.1 × 1.2 @ 34
J1846-0651	18 46 06.3006	-06 51 27.749	3.0	0.021		2.0 × 1.2 @ 30
G028.83-00.25	18 44 51.0841	-03 45 48.406		2.5	81.1	4.2 × 2.2 @ -11
J1834-0301	18 34 14.0746	-03 01 19.627	2.8	0.060		4.7 × 2.3 @ -5
J1833-0323	18 33 23.9050	-03 23 31.446	2.9	0.032		4.8 × 2.1 @ -5
J1846-0651	18 46 06.3004	-06 51 27.747	3.1	0.016		4.9 × 2.0 @ -3
J1853-0048	18 53 41.9894	-00 48 54.321	3.7	0.009		4.4 × 1.9 @ -8
G030.19-00.16	18 47 03.0698	-02 30 36.268		9.2	108.4	4.2 × 2.2 @ -11
J1853-0048	18 53 41.9893	-00 48 54.320	2.4	0.022		4.4 × 2.1 @ -7
J1834-0301	18 34 14.0746	-03 01 19.626	3.2	0.085		4.5 × 2.1 @ -6
J1857-0048	18 57 51.3588	-00 48 21.935	3.2	0.043		4.9 × 1.9 @ -4
J1846-0003	18 46 03.7822	-00 03 38.255	2.5	0.048		4.4 × 2.1 @ -7
G031.28-00.06	18 48 12.38947	-01 26 30.6860		5.0	110.7	5.2 × 3.6 @ 19
J1853-0048	18 53 41.9894	-00 48 54.322	1.5	0.018		5.5 × 3.5 @ -12
J1834-0301	18 34 14.0746	-03 01 19.628	3.8	0.068		5.3 × 3.6 @ 0
J1857-0048	18 57 51.3588	-00 48 21.937	2.5	0.043		5.1 × 3.5 @ -7
J1846-0003	18 46 03.7822	-00 03 38.257	1.5	0.039		4.9 × 3.4 @ -5
G033.39+00.00	18 52 14.6407	+00 24 52.424		3.4	104.6	5.3 × 1.7 @ -19
J1853-0048	18 53 41.9895	-00 48 54.320	1.3	0.015		4.9 × 1.8 @ -13
J1846-0003	18 46 03.7824	-00 03 38.255	1.6	0.037		4.4 × 2.1 @ -12
J1848+0138	18 48 21.8105	+01 38 26.629	1.6	0.028		5.0 × 2.0 @ -14

**Notes.**  $\phi$  is the angular separation between the maser and the calibrator. The maser absolute position, the peak brightness, the size, and the P.A. of the naturally weighted (NW) beam are listed for the first epoch for each source. The P.A. of the beam is defined as east of north.

<sup>a</sup> Methanol maser.

<sup>b</sup> Water maser.

## Appendix B Parallax Fits

Tables 4 and 5 present the detailed results of parallax and proper motion for CH<sub>3</sub>OH and H<sub>2</sub>O maser measurement, respectively. For these masers, all epochs except the ones in brackets in Table 2 are used to fit parallax and proper motion. In the tables, the uncertainties of the proper motions are the formal uncertainty. For masers with only one background source used to fit parallax, in order to compensate for the wedge effect that could not be determined we used 3 times the formal uncertainty as the parallax uncertainty.

**Table 4**  
Details of Methanol Maser Fits

$V_{\text{LSR}}$ (km s <sup>-1</sup> )	Parallax (mas)	$\mu_x$ (mas yr <sup>-1</sup> )	$\mu_y$ (mas yr <sup>-1</sup> )
G000.31–00.20; QSOs: J1748+J1752			
15.5	0.358 ± 0.044	0.35 ± 0.26	–1.73 ± 0.48
16.6	0.323 ± 0.076	0.01 ± 0.46	–1.90 ± 0.74
18.4	0.330 ± 0.032	0.27 ± 0.24	–1.76 ± 0.59
Combined fit	0.342 ± 0.042		
Average		0.21 ± 0.32	–1.76 ± 0.60
G009.21–00.20; QSOs: J1755+J1808+J1819			
40.5	0.318 ± 0.173	–0.37 ± 0.40	–1.78 ± 0.43
41.8	0.331 ± 0.166	–0.49 ± 0.44	–1.77 ± 0.43
45.5	0.371 ± 0.167	–0.49 ± 0.38	–1.66 ± 0.48
45.7	0.353 ± 0.176	–0.29 ± 0.42	–1.57 ± 0.49
Combined fit	0.303 ± 0.096		
Average		–0.41 ± 0.41	–1.69 ± 0.46
G010.32–00.15; QSOs: J1808+J1821+J1751			
13.4	0.273 ± 0.095	–1.24 ± 0.28	–2.90 ± 0.60
13.1	0.213 ± 0.095	–0.88 ± 0.26	–2.62 ± 0.64
12.7	0.186 ± 0.090	–1.21 ± 0.29	–3.14 ± 0.70
10.5	0.131 ± 0.074	–1.32 ± 0.34	–2.58 ± 0.55
10.2	0.130 ± 0.072	–1.49 ± 0.32	–2.78 ± 0.56
9.8	0.193 ± 0.094	–1.28 ± 0.31	–2.88 ± 0.57
9.5	0.254 ± 0.110	–0.89 ± 0.32	–2.68 ± 0.57
6.6	0.181 ± 0.091	–1.16 ± 0.30	–2.83 ± 0.54
6.3	0.185 ± 0.093	–1.16 ± 0.26	–2.67 ± 0.49
5.5	0.263 ± 0.111	–1.01 ± 0.26	–3.17 ± 0.66
4.5	0.196 ± 0.096	–0.86 ± 0.26	–2.96 ± 0.56
4.1	0.191 ± 0.093	–0.84 ± 0.26	–2.85 ± 0.63
Combined fit	0.158 ± 0.076		
Average		–1.08 ± 0.29	–2.84 ± 0.59
G010.34–00.14; QSOs: J1808+J1819+J1821			
4.9	0.381 ± 0.063	–0.94 ± 0.17	–1.87 ± 0.65
10.3	0.362 ± 0.058	–1.04 ± 0.15	–1.90 ± 0.70
10.6	0.357 ± 0.058	–1.01 ± 0.17	–1.98 ± 0.57
12.8	0.368 ± 0.058	–1.04 ± 0.17	–1.79 ± 0.57
16.0	0.371 ± 0.070	–1.02 ± 0.18	–1.79 ± 0.63
Combined fit	0.374 ± 0.040		
Average		–1.01 ± 0.17	–1.87 ± 0.62
G011.10–00.11; QSOs: J1751+J1821			
29.8	0.251 ± 0.036	–0.21 ± 0.32	–2.09 ± 0.40
30.2	0.234 ± 0.043	–0.30 ± 0.38	–2.03 ± 0.38
32.0	0.251 ± 0.041	–0.20 ± 0.32	–1.87 ± 0.35
Combined fit	0.246 ± 0.014		
Average		–0.23 ± 0.35	–2.01 ± 0.38
G018.87+00.05; QSO: J1821–1224			
38.3	0.297 ± 0.016	–0.17 ± 0.07	–1.90 ± 0.20
G019.36–00.03; QSO: J1821–1224			
25.4	0.353 ± 0.034	–1.19 ± 0.44	–3.22 ± 0.46

**Table 4**  
(Continued)

$V_{\text{LSR}}$ (km s <sup>-1</sup> )	Parallax (mas)	$\mu_x$ (mas yr <sup>-1</sup> )	$\mu_y$ (mas yr <sup>-1</sup> )
27.2	0.342 ± 0.020	–1.10 ± 0.27	–3.04 ± 0.39
28.6	0.361 ± 0.018	–1.07 ± 0.22	–3.06 ± 0.34
Combined fit	0.352 ± 0.023		
Average		–1.12 ± 0.31	–3.11 ± 0.40
G022.03+00.22; QSO: J1825–0737			
49.5	0.333 ± 0.032	–0.12 ± 0.21	–1.54 ± 0.40
51.7	0.331 ± 0.020	–0.12 ± 0.14	–1.51 ± 0.56
53.3	0.324 ± 0.015	0.00 ± 0.09	–1.75 ± 0.56
54.4	0.340 ± 0.024	0.00 ± 0.16	–1.48 ± 0.63
Combined fit	0.332 ± 0.018		
Average		–0.06 ± 0.15	–1.57 ± 0.54
G024.63–00.32; QSOs: J1825+J1846			
35.7	0.196 ± 0.049	0.07 ± 0.24	–2.84 ± 0.28
48.1	0.306 ± 0.142	–0.67 ± 0.22	–2.62 ± 0.24
Combined fit	0.242 ± 0.045		
Average		–0.31 ± 0.22	–2.73 ± 0.26
G028.30–00.38; QSOs: J1833+J1834+J1846			
81.3	0.226 ± 0.029	–1.64 ± 0.17	–3.90 ± 0.19
82.0	0.221 ± 0.031	–1.77 ± 0.20	–4.13 ± 0.22
82.4	0.210 ± 0.029	–1.55 ± 0.18	–4.02 ± 0.19
92.4	0.193 ± 0.032	–1.54 ± 0.20	–4.01 ± 0.21
93.9	0.257 ± 0.027	–1.61 ± 0.16	–3.83 ± 0.18
Combined fit	0.221 ± 0.022		
Average		–1.62 ± 0.18	–3.97 ± 0.19
G028.39+00.08; QSOs: J1833+J1834+J1846			
69.1	0.212 ± 0.021	–1.38 ± 0.07	–3.34 ± 0.10
71.3	0.209 ± 0.019	–1.43 ± 0.06	–3.33 ± 0.07
81.7	0.229 ± 0.020	–1.41 ± 0.06	–3.15 ± 0.09
Combined fit	0.219 ± 0.013		
Average		–1.40 ± 0.06	–3.26 ± 0.08
G028.83–00.25; QSOs: J1833+J1834+J1846+J1853			
81.1	0.185 ± 0.049	–1.90 ± 0.19	–4.47 ± 0.17
90.8	0.219 ± 0.049	–1.89 ± 0.18	–4.62 ± 0.21
Combined fit	0.200 ± 0.040		
Average		–1.89 ± 0.18	–4.54 ± 0.19
G030.19–00.16; QSOs: J1834+J1846+J1853+J1857			
104.8	0.202 ± 0.016	–1.98 ± 0.21	–3.76 ± 0.19
108.4	0.226 ± 0.014	–2.08 ± 0.17	–3.96 ± 0.23
109.4	0.220 ± 0.014	–2.13 ± 0.17	–3.69 ± 0.21
109.4	0.190 ± 0.017	–1.99 ± 0.26	–3.60 ± 0.26
109.4	0.239 ± 0.015	–2.10 ± 0.17	–3.86 ± 0.18
110.2	0.198 ± 0.013	–2.12 ± 0.13	–3.97 ± 0.25
Combined fit	0.212 ± 0.010		
Average		–2.08 ± 0.17	–3.80 ± 0.21
G031.28+00.06; QSOs: J1834+J1846+J1853+J1857			
105.7	0.176 ± 0.041	–2.13 ± 0.09	–5.01 ± 0.29
106.0	0.248 ± 0.069	–2.16 ± 0.18	–4.85 ± 0.27
107.5	0.235 ± 0.061	–1.87 ± 0.15	–4.65 ± 0.27
110.0	0.179 ± 0.065	–2.10 ± 0.15	–4.73 ± 0.31
110.4	0.263 ± 0.068	–2.11 ± 0.16	–4.73 ± 0.25
110.4	0.134 ± 0.053	–1.66 ± 0.15	–4.57 ± 0.30
110.7	0.223 ± 0.044	–1.75 ± 0.11	–4.88 ± 0.26
111.1	0.088 ± 0.046	–1.27 ± 0.15	–4.75 ± 0.28
Combined fit	0.179 ± 0.045		
Average		–1.86 ± 0.14	–4.78 ± 0.28
G033.39+00.00; QSOs: J1846+J1848+J1853			
98.2	0.118 ± 0.044	–2.61 ± 0.11	–5.36 ± 0.12
105.4	0.112 ± 0.038	–2.41 ± 0.10	–5.33 ± 0.09
106.1	0.114 ± 0.036	–2.40 ± 0.12	–5.38 ± 0.11
Combined fit	0.113 ± 0.029		
Average		–2.48 ± 0.11	–5.36 ± 0.11

**Table 5**  
Details of Water Maser Fit

Background Source	$V_{\text{LSR}}$ ( $\text{km s}^{-1}$ )	Parallax (mas)	$\mu_x$ ( $\text{mas yr}^{-1}$ )	$\mu_y$ ( $\text{mas yr}^{-1}$ )
G28.39+0.08				
J1833–0323	77.5	$0.304 \pm 0.009$	$-1.42 \pm 0.02$	$-2.61 \pm 0.17$
	77.6	$0.268 \pm 0.029$	$-2.12 \pm 0.08$	$-2.71 \pm 0.15$
	78.7	$0.452 \pm 0.028$	$-1.14 \pm 0.07$	$-1.62 \pm 0.18$
	Combined fit Average	$0.331 \pm 0.047$	$-1.56 \pm 0.06$	$-2.31 \pm 0.17$
J1834–0301	77.5	$0.211 \pm 0.040$	$-1.32 \pm 0.10$	$-2.55 \pm 0.19$
	77.6	$0.152 \pm 0.033$	$-1.93 \pm 0.09$	$-2.66 \pm 0.19$
	78.7	$0.364 \pm 0.034$	$-1.04 \pm 0.09$	$-1.56 \pm 0.19$
	Combined fit Average	$0.243 \pm 0.054$	$-1.43 \pm 0.09$	$-2.25 \pm 0.19$
J1846–0651	77.5	$0.207 \pm 0.032$	$-1.48 \pm 0.08$	$-2.63 \pm 0.20$
	77.6	$0.170 \pm 0.024$	$-2.16 \pm 0.07$	$-2.68 \pm 0.23$
	78.7	$0.356 \pm 0.051$	$-1.20 \pm 0.13$	$-1.63 \pm 0.23$
	Combined fit Average	$0.247 \pm 0.054$	$-1.60 \pm 0.09$	$-2.31 \pm 0.22$
Combined fit Average		$0.272 \pm 0.031$	$-1.53 \pm 0.08$	$-2.29 \pm 0.19$

### ORCID iDs

M. J. Reid  <https://orcid.org/0000-0001-7223-754X>  
A. Sanna  <https://orcid.org/0000-0001-7960-4912>  
Y. Xu  <https://orcid.org/0000-0001-5602-3306>  
B. Zhang  <https://orcid.org/0000-0003-1353-9040>  
A. Brunthaler  <https://orcid.org/0000-0003-4468-761X>  
K. M. Menten  <https://orcid.org/0000-0001-6459-0669>

### References

Dame, T. M., Hartmann, D., & Thaddeus, P. 2001, *ApJ*, 547, 792  
Fomalont, E. B., Petrov, L., MacMillan, D. S., et al. 2003, *AJ*, 126, 2562  
Immer, K., Brunthaler, A., Reid, M. J., et al. 2011, *ApJS*, 194, 25

Immer, K., Li, J., Quiroga-Nuñez, L. H., et al. 2019, *A&A*, 632, A123  
Moscadelli, L., Menten, K. M., Walmsley, C. M., et al. 2002, *ApJ*, 564, 813  
Petrov, L., Kovalev, Y. Y., Fomalont, E., et al. 2005, *AJ*, 129, 1163  
Reid, M. J., Brunthaler, A., Menten, K. M., et al. 2017, *AJ*, 154, 63  
Reid, M. J., Menten, K. M., Brunthaler, A., et al. 2009, *ApJ*, 693, 397  
Reid, M. J., Menten, K. M., Brunthaler, A., et al. 2014, *ApJ*, 783, 130  
Reid, M. J., Menten, K. M., Brunthaler, A., et al. 2019, *ApJ*, 885, 131  
Sanna, A., Moscadelli, L., Cesaroni, R., et al. 2010, *A&A*, 517, A78  
Sato, M., Wu, Y. W., Immer, K., et al. 2014, *ApJ*, 793, 72  
VERA Collaboration, Hirota, T., Nagayama, T., et al. 2020, *PASJ*, 72, 50  
Wegg, C., Gerhard, O., & Portail, M. 2015, *MNRAS*, 450, 4050  
Xu, Y., Reid, M. J., Menten, K. M., et al. 2006a, *ApJS*, 166, 526  
Xu, Y., Reid, M. J., Zheng, X. W., et al. 2006b, *Sci*, 311, 54  
Zhang, B., Moscadelli, L., Sato, M., et al. 2014, *ApJ*, 781, 89  
Zhang, B., Reid, M. J., Zhang, L., et al. 2019, *AJ*, 157, 200